

Multi-Branch Generative Models for Multichannel Imaging with an Application to PET/CT Synergistic Reconstruction

Noel Jeffrey Pinton, Alexandre Bousse, *Member, IEEE*, Catherine Cheze-Le-Rest, Dimitris Visvikis, *Senior Member, IEEE*

Abstract—This paper presents a novel approach for learned synergistic reconstruction of medical images using multi-branch generative models. Leveraging variational autoencoders (VAEs), our model learns from pairs of images simultaneously, enabling effective denoising and reconstruction. Synergistic image reconstruction is achieved by incorporating the trained models in a regularizer that evaluates the distance between the images and the model. We demonstrate the efficacy of our approach on both Modified National Institute of Standards and Technology (MNIST) and positron emission tomography (PET)/computed tomography (CT) datasets, showcasing improved image quality for low-dose imaging. Despite challenges such as patch decomposition and model limitations, our results underscore the potential of generative models for enhancing medical imaging reconstruction.

Index Terms—Multi-branch Generative Models, Multichannel Imaging, Synergistic Reconstruction

I. INTRODUCTION

MULTIMODAL imaging refers to acquiring data from different sources or from different techniques to capture complementary information about the object or scene being observed. Multimodal imaging is used in various fields such as remote sensing [1], [2] robotics [3], [4] and medical imaging [5], [6]. Some of the modalities used in the latter field include PET, CT, magnetic resonance imaging (MRI), ultrasound, and various optical imaging techniques. PET is a powerful medical imaging technique that uses a small amount of radioactive material to visualize and track various processes in the body. It provides valuable insights into cancer detection and other areas of medicine such as cardiology and neurology [7]. PET is often completed with CT and MRI which provide anatomical information.

Images are reconstructed by solving modality-specific inverse problems. In medical imaging, early methods were based on inversion formulas such as filtered backprojection [8] for CT and PET as well as inverse fast Fourier transform for MRI. These methods were then followed by model-based iterative reconstruction (MBIR) algorithms which consist of iteratively

minimizing a cost function comprising a data fidelity term that encompasses the physics and statistics of the measurement and a regularizer to control the noise. Such methods include expectation-maximization for PET and single-photon emission CT (SPECT) [9] and its regularized versions [10], [11], as well as penalized weighted least squares (WLS) for CT [12].

Multimodal imaging systems produce multiple images of the same underlying object. In general, each modality is reconstructed individually. However, they correspond to images of the same object. Therefore, it is natural to take advantage of the inter-modality information to reconstruct the images together, or *synergistically*, in order to improve the signal-to-noise ratio (SNR). In medical imaging, this approach can give room for dose reduction and/or scan time reduction.

Early synergistic techniques use handcrafted multichannel regularizers embedded within a MBIR framework, such as joint total variation (JTV) for color images [13] and PET/MRI [14], the parallel level set (PLS) prior for PET/MRI [15] and total nuclear variation (TNV) for multi-energy (or spectral) CT [16] (see [17] for a review). These handcrafted regularizers promote structural similarities between the images, and therefore may not be suitable for modalities with different intrinsic resolution. For example, in PET/CT or PET/MRI, the resolution of the PET can be artificially enhanced, and while this enhancement may improve aesthetics and quantification in applications such as brain PET/MRI [18], it may not accurately represent the actual distribution of radiotracers the rest of the body where higher sensitivity is required at the expense of spatial resolution (e.g., metastases detection).

Alternatively, the inter-modality information can be learned with machine learning (ML) techniques. Dictionary learning (DiL) techniques have been used in image reconstruction for single-energy CT [19] but also for spectral CT through tensor DiL to sparsely represent the images in a joint multidimensional dictionary [20]–[23] (see [24] for a review). A similar multichannel DiL approach was proposed for PET/MRI [25]. All these works reported better performances using multichannel DiL as compared with single-channel DiL. DiL relies on patch decomposition, which is not efficient for joint sparse representation across channels. To remedy this, multichannel convolutional DiL was proposed (see [26] for dual-energy CT).

Multichannel DiL is limited to encoding structural information only. In that sense, synergistic multichannel image reconstruction could benefit from the deeper architectures used in deep learning (DL). However, few researchers addressed

This work did not involve human subjects or animals in its research.

This work was supported by the French National Research Agency (ANR) under grant No ANR-20-CE45-0020 and by France Life Imaging under grant No ANR-11-INBS-0006

All authors are with Univ. Brest, LaTIM, INSERM, UMR 1101, 29238 Brest, France.

C. Cheze-Le-Rest is also with Nuclear Medicine Department, Poitiers University Hospital, F-86022, Poitiers, France.

Corresponding authors: A. Bousse, bousse@univ-brest.fr

synergistic reconstruction using DL. For example in a recent work, Corda-D’Incan *et al.* [27] proposed an unrolling framework for synergistic PET/MRI reconstruction. The training of unrolling models is supervised and computationally expensive as it integrates the imaging system forward model at each layer.

In this work, which is an extension of our previous work [28], [29], we investigate the feasibility of DL for synergistic multichannel image reconstruction through the utilization of a deep generative model (i.e., a VAE) incorporated within a MBIR framework through a regularizer in a similar fashion as proposed by Duff *et al.* [30] (and to some extent Kelkar *et al.* [31]). For our approach, we used multiple-branch generators to map a single latent variable to multiple images. The training is unsupervised and performed on an image pair basis and does not involve the forward model, thus enabling the possibility to use the same model to any imaging system using the same modalities.

In Section II we present our multi-branch VAE (MVAE) architecture and the corresponding reconstruction algorithm. Section III demonstrates the capability of our architectures to generate multiple images and to convey information across channels, and shows the results of their utilization in a denoising framework with data generated from the MNIST database [32] and in for synergistic PET/CT reconstruction with a comparison with the PLS technique [15]. Section IV discusses the limitations of our method and experiments. Finally, Section V concludes this paper.

II. METHOD

A. Background on Medical Image Reconstruction

Image reconstruction corresponds to the task of estimating an image $\mathbf{x} \in \mathcal{X} \triangleq \mathbb{R}^m$ from a random measurement $\mathbf{y} \in \mathcal{Y} \triangleq \mathbb{R}^n$, where m and n are respectively the dimension of the image (number of pixels or voxels) and the dimension of the measurement (number of detectors). The image \mathbf{x} is a visual representation of the interior of an object (e.g., the patient).

The measurement is modeled with a forward model which takes the form of a mapping $\bar{\mathbf{y}}: \mathcal{X} \rightarrow \mathcal{Y}$ that incorporates the physics of the measurement such that given a ground truth (GT) image \mathbf{x}^* the expected measurement matches the forward model, i.e., $\mathbb{E}[\mathbf{y}] = \bar{\mathbf{y}}(\mathbf{x}^*)$. When the measurement consists of photon counting (e.g., PET, SPECT and CT), \mathbf{y} is a random vector that follows a Poisson distribution with independent entries, i.e.,

$$\mathbf{y} \sim \text{Poisson}(\bar{\mathbf{y}}(\mathbf{x}^*)). \quad (1)$$

The forward model $\bar{\mathbf{y}}$ depends on the imaging system. In PET, it is traditionally written as

$$\bar{\mathbf{y}}(\mathbf{x}) = \tau(\mathbf{P}\mathbf{x} + \mathbf{r}) \quad (2)$$

where \mathbf{x} is the radiotracer distribution image, $\mathbf{P} \in \mathbb{R}^{n \times m}$ is the PET system matrix such that each entry $[\mathbf{P}]_{i,j}$ is the probability that a positron-electron annihilation in voxel j is detected by the i th detector pair (with incorporation of the attenuation factors, resolution and sensitivity), τ is the acquisition time and $\mathbf{r} \in \mathbb{R}^n$ is a “background term” representing the expected

scatter and randoms per unit of time. In CT, the standard (monochromatic) model is

$$\bar{\mathbf{y}}(\mathbf{x}) = I \cdot \exp(-\mathbf{A}\mathbf{x}) \quad (3)$$

where \mathbf{x} is the attenuation image, $\mathbf{A} \in \mathbb{R}^{n \times m}$ is the CT system matrix, I is the X-ray intensity and the \exp function applied to a vector should be understood as operating on each element individually.

Image reconstruction is achieved by matching $\bar{\mathbf{y}}(\mathbf{x})$ to \mathbf{y} , i.e.,

$$\text{find } \mathbf{x} \text{ s.t. } \bar{\mathbf{y}}(\mathbf{x}) \approx \mathbf{y}, \quad (4)$$

which is an (ill-posed) inverse problem. As solving (4) cannot be achieved with an inversion formula without amplifying the noise, MBIR techniques have been prevalent over the last decades. MBIR consists in solving an optimization problem of the form

$$\min_{\mathbf{x} \in \mathcal{X}} L(\mathbf{y}, \bar{\mathbf{y}}(\mathbf{x})) + \beta R(\mathbf{x}) \quad (5)$$

where L is a loss function that evaluates the goodness of fit between the measurement \mathbf{y} and the expectation $\bar{\mathbf{y}}$, $R: \mathcal{X} \rightarrow \mathbb{R}$ is a regularizer, and $\beta > 0$ is a weight, with an iterative algorithm. The loss function L is usually defined a negative Poisson log-likelihood, although it can be approximated by a WLS loss (see for example [12] in CT). The regularizer R promotes images that have desired properties, such as piecewise smoothness or sparsity of the gradient.

The choice of the algorithm to solve (5) largely depends on $\bar{\mathbf{y}}$, L , and R . Examples from the literature include separable paraboloidal surrogates (SPS) for CT [12], maximum-likelihood expectation-maximization (MLEM), ordered subsets expectation maximization [9], [33] and modified MLEM [11] for PET with smooth regularizers. Non-smooth regularizers can be addressed for example with a primal-dual algorithm [34].

B. Synergistic Reconstruction in Multimodal Imaging

Multimodal hybrid imaging systems such as PET/CT, PET/MRI, SPECT/CT (and to some extent, spectral CT) can acquire multiple measurement $\{\mathbf{y}_k\} = \{\mathbf{y}_1, \dots, \mathbf{y}_K\}$, $\mathbf{y}_k \in \mathbb{R}^{n_k} \triangleq \mathcal{Y}_k$, to reconstruct several images $\{\mathbf{x}_k\} = \{\mathbf{x}_1, \dots, \mathbf{x}_K\}$. For simplicity, we assume that the images \mathbf{x}_k are all m -dimensional. In general, each channel k is individually reconstructed by solving (5) using its corresponding forward model $\bar{\mathbf{y}}_k: \mathcal{X} \rightarrow \mathcal{Y}_k$, loss function $L_k: \mathcal{Y}_k \times \mathcal{Y}_k \rightarrow \mathbb{R}$ and regularizer R_k . Another approach consists of reconstructing the images simultaneously by solving

$$\min_{\{\mathbf{x}_k\} \in \mathcal{X}^K} \sum_{k=1}^K \eta_k L_k(\mathbf{y}_k, \bar{\mathbf{y}}_k(\mathbf{x}_k)) + \beta R_{\text{syn}}(\mathbf{x}_1, \dots, \mathbf{x}_K) \quad (6)$$

where $R_{\text{syn}}: \mathcal{X}^K \rightarrow \mathbb{R}$ is a *synergistic* regularizer that promotes structural and/or functional dependencies between the multiple images and the η_k s are positive normalized weights ($\eta_k > 0$, $\sum_k \eta_k = 1$) that tune the strength of the regularizer for each channel k independently¹.

¹In (6) the weight β may also be incorporated in the η_k s. However, in this work, it is more convenient to keep them separated, cf. footnote in Section II-D.

A classical regularizer is JTV [13] which encourages joint sparsity of the image gradients. Similarly, TNV, which encourages common edge locations and a shared gradient direction among image channels, was used in spectral CT [16]. Another example is the PLS prior which was used in PET/MRI [15]. By promoting common features between the images, synergistic regularizers can convey information across channels in a way that each image \mathbf{x}_k leverages the entire raw data $\mathbf{y}_1, \dots, \mathbf{y}_K$, thus improving the SNR. However, enforcing structural similarities may not be appropriate for modalities that do not have the same intrinsic resolutions, such as in PET/CT and PET/MRI.

C. Learned Regularizers with Generative Models

ML and DL techniques have been used in inverse problem-solving and image reconstruction [35]. These approaches have changed the paradigm of image reconstruction in the sense that they are trained to deliver the reconstructed images. For example, unrolling methods extend conventional iterative algorithms into a deep architecture for end-to-end reconstructions [36], while other techniques directly map the raw data into the image space [37]–[39]. Another category of technique aims at training a penalty $R_\theta: (\mathbb{R}^m)^K \rightarrow \mathbb{R}$ with respect to some parameter θ such that it promotes plausible multichannel image $\{\mathbf{x}_k\}$, that is to say, images that are plausible not only individually but also together.

1) *Proposed Regularizer*: This section focuses on generative model-based regularizers, i.e., based on a multichannel image patch generator $\mathbf{G}_\theta^{\text{mult}}$ with trainable parameter θ , of the form

$$\mathbf{G}_\theta^{\text{mult}} \triangleq \{\mathbf{G}_\theta^1, \dots, \mathbf{G}_\theta^K\}: \mathcal{Z} \rightarrow \mathcal{U}^K \quad (7)$$

where for each $k = 1, \dots, K$, $\mathbf{G}_\theta^k: \mathcal{Z} \rightarrow \mathcal{U}$ is a generative model that maps a latent variable \mathbf{z} in the latent space $\mathcal{Z} \triangleq \mathbb{R}^s$ to a d -dimensional image, $d < m$, corresponding to a patch (a portion of an image) in channel k , and $\mathcal{U} = \mathbb{R}^d$ is the patch space. The s -dimensional latent variable \mathbf{z} , $s < d$, encodes the information of the image patch. Note that $\mathbf{G}_\theta^{\text{mult}}$ takes a single \mathbf{z} as input such that the K images correspond to the same \mathbf{z} .

We used a patch decomposition with overlaps to reduce training complexity and minimize hallucinations. Hallucinations arise when the generative model produces outputs that are not constrained by the range-space of the training data, leading to artifacts or erroneous features in the generated images. By using overlapping patches, the effect of local hallucinations in a patch are averaged out by neighboring patches.

In the following, $\mathbf{P}_p: \mathcal{X} \rightarrow \mathcal{U}$ is the p th patch extractor, $p = 1, \dots, P$, such that for each channel k , $\mathbf{u}_k = \mathbf{P}_p \mathbf{x}_k \in \mathcal{U}$ is a ‘‘portion’’ of \mathbf{x}_k . The patches cover the entire image, with possible overlaps. The corresponding synergistic regularizer R_θ is then defined as

$$R_\theta(\{\mathbf{x}_k\}) \triangleq \min_{\{\mathbf{z}_p\} \in \mathcal{Z}^P} \sum_{p=1}^P \sum_{k=1}^K \frac{\eta_k}{2} \left\| \mathbf{G}_\theta^k(\mathbf{z}_p) - \mathbf{P}_p \mathbf{x}_k \right\|^2 + \alpha H(\mathbf{z}_p) \quad (8)$$

where H is a regularizer on the latent variable with weight $\alpha > 0$ and the η_k are the same as in (6). The regularizer R_θ is

minimized when for all patch p , each $\mathbf{P}_p \mathbf{x}_k$, $k = 1, \dots, L$, is approximately generated from a same \mathbf{z}_p that is ‘regularized’ in the sense of H . Solving the penalized maximum likelihood (PML) problem (6) with $R_{\text{syn}} = R_\theta$ requires to alternate minimization in $\{\mathbf{z}_p\}$ and $\{\mathbf{x}_k\}$. The penalty R_θ allows some flexibility for the solution in the sense that the reconstructed image patches (i.e., obtained by solving (6)) are not necessarily in the range of $\mathbf{G}_\theta^{\text{mult}}$. Another approach discussed in Duff *et al.* [30] consists in imposing the images to be in the range of $\mathbf{G}_\theta^{\text{mult}}$. However, minimizing this regularizer is unpractical when using overlapping patches.

2) *Proposed Generative Model*: In this work we propose to utilize a multichannel image generator $\mathbf{G}_\theta: \mathcal{Z} \rightarrow \mathcal{U}^K$ trained as a MVAE with a multi-branch architecture inspired from Duff *et al.* [30] and Wang *et al.* [40]. While standard VAEs are trained with a single encoder and a single generator (or decoder), our MVAE uses a multi-branch encoder mapping the K channels to a single latent variable \mathbf{z} which is then mapped to K images with $\mathbf{G}_\theta = \{\mathbf{G}_\theta^k, k = 1, \dots, K\}$ with a multi-branch decoder. Details on the training are given in Appendix B. In contrast with multi-channel single-branch models, multi-branch generative models introduce parallel pathways, each specializing in generating specific components of the data. By implementing this segregation, the original attributes unique to each modality can be better preserved in both the encoding and decoding components with minimal cross-talk, with interactions only taking place within the latent space.

The MVAE architecture for $K = 2$, 32×32 patches, and $s = 32$ is represented in Figure 1. In this work, we employed a four-layer convolutional NN network for the encoder and decoder branches with rectified linear unit [41] activation. All encoder branches have identical architecture and the same principle is also applied to all decoder branches. The VAE network was trained on bimodal ($K = 2$) image pairs with little to no processing on the original image. The model is designed to be trained on matching images, such that it can learn to convey information from one image to another. In the PET/CT case, the image pairs need to be co-registered as patient motion and respiratory motion may cause misalignment between the PET and the CT which may affect the training.

D. Reconstruction Algorithm

Solving (6) using the synergistic regularizer $R_{\text{syn}} = R_\theta$ defined in (8) is achieved by alternating minimization in $\{\mathbf{z}_p\}$ and $\{\mathbf{x}_k\}$. Given a current estimate $\mathbf{x}_k^{(q)}$ at iteration q , the new estimate at iteration $q + 1$ is given by

$$\begin{aligned} \mathbf{z}_p^{(q)} &= \arg \min_{\mathbf{z} \in \mathcal{Z}} \sum_{k=1}^K \frac{\eta_k}{2} \left\| \mathbf{G}_\theta^k(\mathbf{z}) - \mathbf{P}_p \mathbf{x}_k^{(q)} \right\|_2^2 + \alpha H(\mathbf{z}) \\ &\quad \forall p = 1, \dots, P \\ \mathbf{x}_k^{(q+1)} &= \arg \min_{\mathbf{x} \in \mathcal{X}} L_k(\mathbf{y}_k, \bar{\mathbf{y}}_k(\mathbf{x})) \\ &\quad + \frac{\beta}{2} \sum_{p=1}^P \left\| \mathbf{G}_\theta^k(\mathbf{z}_p^{(q)}) - \mathbf{P}_p \mathbf{x} \right\|_2^2 \quad \forall k = 1, \dots, K \end{aligned} \quad (9)$$

(10)

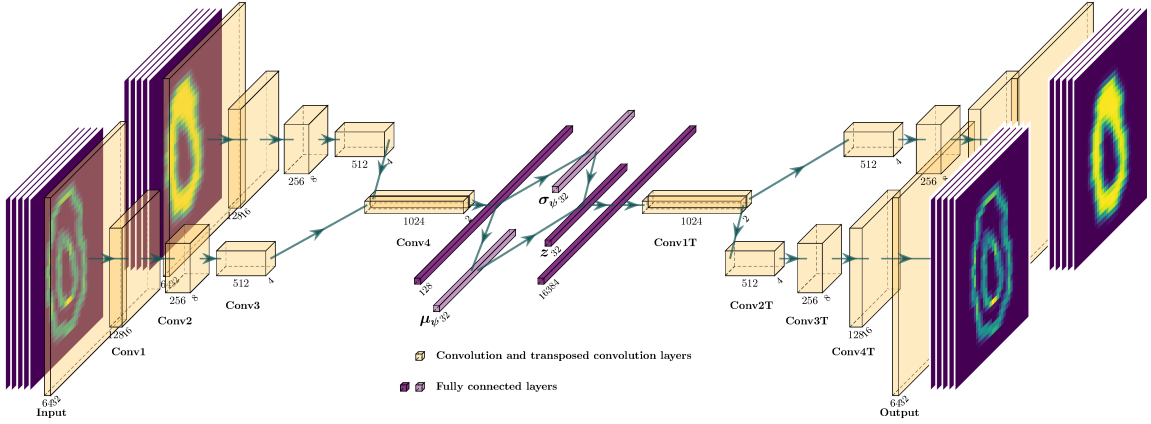


Fig. 1: Architecture of our proposed MVAE.

Both sub-minimizations can be achieved with iterative algorithms initialized from the previous estimates $z_p^{(q)}$ and $x_k^{(q)}$. The x -update (10) depends on the loss L_k and the forward model \tilde{y}_k^2 . For PET/CT reconstruction, we used a modified MLEM algorithm [42] for the PET update (10 sub-iterations) while used using a SPS algorithm [12] for the CT update (10 sub-iterations). Note that it is possible to use different β -values for each k in (10) to adjust the strength of R_θ for each channel. Finally, we implemented the z -update step (9) with a limited-memory Broyden-Fletcher-Goldfarb-Shanno (L-BFGS) algorithm [43] (50 sub-iterations). A total of 20 outer-iterations was used.

III. RESULTS

In this section, we show some results of our methodology for $K = 2$. Section III-A presents an evaluation based on the MNIST image dataset [32] (resized to 32×32), while Section III-B presents results for PET/CT joint reconstruction from synthetic projection data generated from real patient images. The two parameters η_1 and η_2 in the optimization problem (6) and the regularizer (8) are rewritten as

$$\eta_1 = \eta \quad \text{and} \quad \eta_2 = 1 - \eta, \quad \eta \in [0, 1]. \quad (11)$$

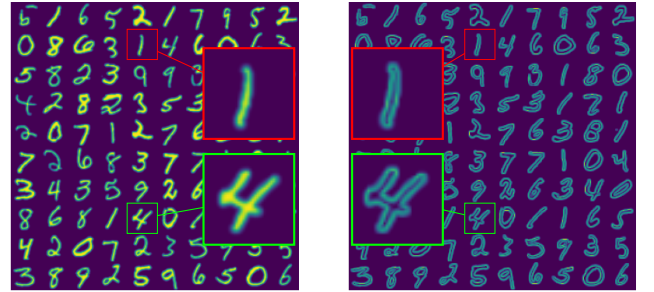
For simplicity, and to solely focus on the inter-channel dependencies, we used $H \equiv 0$, i.e., no regularization on z . Our generative model-based regularizer simplifies to

$$R_\theta(x_1, x_2) = \min_{\{z_p\} \in \mathcal{Z}^P} \left(\sum_{p=1}^P \frac{\eta}{2} \left\| G_\theta^1(z_p) - P_p x_1 \right\|^2 + \frac{1-\eta}{2} \left\| G_\theta^2(z_p) - P_p x_1 \right\|^2 \right). \quad (12)$$

While we used a range of η -values for MNIST, we used $\eta = 1/2$ for PET/CT.

The quality of the reconstructed images was assessed using the peak signal-to-noise ratio (PSNR) and structural similarity

²The minimization w.r.t. x_k (10) does not depend on η_k as each loss L_k is multiplied by η_k in (6)



(a) x_1 images

(b) x_2 images

Fig. 2: Example of x_1, x_2 image pairs derived from the MNIST dataset used to train the MVAE model.

index measure (SSIM) with respect to the GT images (x_1^*, x_2^*). We used the functions `peak_signal_noise_ratio` and `structural_similarity` from the Python package `skimage.metrics` to compute the PSNR and SSIM. The training of the architectures was implemented on a single Nvidia RTX A6000 GPU.

A. MNIST Data

1) *Data and Training*: The database consists of a collection of 70,000 32×32 image pairs representing digits from 0 to 9 with various shapes (see Figure 2(a)). These images play the role of the first channel, i.e., x_1 . The second channel images x_2 are derived from x_1 using a Roberts edge detection filter from `scikit-image` [44] followed by a Gaussian filter. Figure 2 shows an example of training image pairs. We used $P = 1$, $d = m = 32^2$, and $P_1 = \text{id}_{\mathcal{X}}$ (identity operator on \mathcal{X}).

The MVAE models were trained in an unsupervised manner using 60,000 image pairs for training and 10,000 image pairs for testing. All models were trained using the Adam optimizer with a learning rate of 10^{-4} . The batch size was chosen experimentally to balance between memory and time constraints and we used batches of 10,240 for 10,000 epochs.

2) Results:

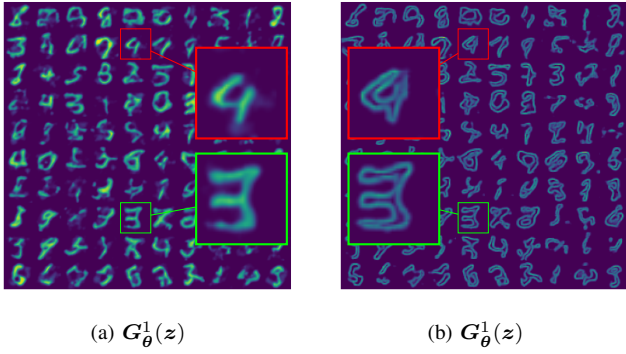


Fig. 3: MVAE-generated image pairs ($G_\theta^1(z), G_\theta^2(z)$), using the MNIST-trained models, with random $z \in \mathcal{Z}$. The sub-images on (a) and (b) at same position were generated from the same z .

a) *Image Generation*: Figures 3 shows generated images using the MVAE model using a random z generated by uniformly sampling each of its coordinates on $[-3, 3]$. The images are distorted digits, similar to the training dataset. We observe that images generated from the same z correspond to each other, which suggests that both generators were able to learn from the pairs as opposed to each image individually.

b) *Image Prediction*: x_1 to x_2 and x_2 to x_1 : We define the “model-fitting” function f_η , which evaluates the goodness of the fit between a pair of target images (x_1^*, x_2^*) and the generated pair from a trained two-channel model ($G_\theta^1(z), G_\theta^2(z)$) as

$$f_\eta(z, x_1^*, x_2^*) \triangleq \eta \|G_\theta^1(z) - x_1^*\|_2^2 + (1 - \eta) \|G_\theta^2(z) - x_2^*\|_2^2 \quad (13)$$

The optimal latent variable, denoted \check{z}_η , is defined as

$$\check{z}_\eta \triangleq \arg \min_{z \in \mathcal{Z}} f_\eta(z, x_1, x_2), \quad (14)$$

where we dropped the (x_1, x_2) -dependency on the left-hand side to lighten the notation. Finally, the “predicted images” are given by

$$\check{x}_k^\eta = G_\theta^k(\check{z}_\eta), \quad k = 1, 2. \quad (15)$$

Thus, $(\check{x}_1^\eta, \check{x}_2^\eta)$ represents the “best copy” of (x_1^*, x_2^*) where the weight η dictates which target image the generative model should prioritize. In particular for $\eta = 0$ the model-fitting process (14) is oblivious to x_1 so that \check{x}_1^0 is a “prediction” of x_1^* from x_2^* using the model (and conversely with $\eta = 1$).

Figure 4 shows MVAE-generated images $(\check{x}_1^\eta, \check{x}_2^\eta)$ obtained using model-fitting to a target MNIST digit pair (x_1^*, x_2^*) (from the testing dataset) for different values of η . When $\eta = 0.5$, both generated images $(\check{x}_1^{0.5}, \check{x}_2^{0.5})$ correspond to the targets with almost no visible mismatch. When $\eta = 1$, \check{x}_1^1 is similar to x_1^* as expected, while \check{x}_2^1 is somehow similar to x_2^* (with some distortions), which shows that the model managed to predict an image fairly similar to x_2^* using x_1^* only. The converse result is observed with $\eta = 0$.

c) *Image Denoising*: In this section, we focus on denoising two noisy images x_1^n and x_2^n ,

$$x_k^n = x_k^* + \epsilon_k, \quad k = 1, 2 \quad (16)$$

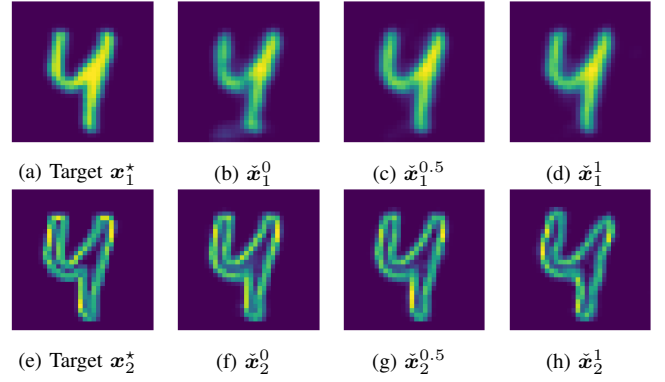


Fig. 4: MVAE-generated images $(\check{x}_1^\eta, \check{x}_2^\eta)$ obtained by model-fitting to a target MNIST digit pair x_1^*, x_2^* for different values of the parameter $\eta \in [0, 1]$ which balances the contribution of each image to the fitting. When $\eta = 0$ (resp. $\eta = 1$), the model-fitting is oblivious of x_1^* (resp. x_2^*) and focuses x_2^* (resp. x_1^*), such that \check{x}_1^0 (resp. \check{x}_2^1) is a prediction of x_1^* (resp. x_2^*) from x_2^* (resp. x_1^*). When $\eta = 0.5$, the model uses x_1^* and x_2^* equally.

where (x_1^*, x_2^*) is a GT image pair (from the testing dataset) and $\epsilon_k \sim \mathcal{N}(\mathbf{0}_m, \sigma_k^2 \text{id}_{\mathcal{X}})$, using a penalized least squares approach, i.e., solving (6) with $\mathbf{y}_k = x_k^n$, $\bar{\mathbf{y}}_k = \text{id}_{\mathcal{X}}$, $L_k(\mathbf{y}_k, \bar{\mathbf{y}}_k) = \frac{1}{2} \|\mathbf{y}_k - \bar{\mathbf{y}}_k\|_2^2$ and using the trained regularizer $R_{\text{syn}} = R_\theta$ defined in (12). As $P = 1$, the image update (10) simplifies to $x_k^{(q+1)} = (1 + \beta)^{-1} (x_k^n + \beta G_\theta^k(z^{(q+1)}))$, $k = 1, 2$. We used $\beta = 1$ and $\sigma_2 > \sigma_1$ in order to assess if the second image benefits from the first.

The denoised images are denoted \hat{x}_1^η and \hat{x}_2^η their corresponding latent encoding is denoted \hat{z}^η . Figure 5 shows the input noisy images x_k^n and the denoised images \hat{x}_k^η . For $\eta = 0$, the model ignores the first channel and focuses on the second channel only, which is the noisiest. Therefore the model fails to generate the second image, which results in a poor prediction for the first image. The quality of \hat{x}_1^η seems to increase as η approaches 0.9 (with a slight decrease at $\eta = 1$). In contrast, the quality of \hat{x}_2^η seems to increase between $\eta = 0$ and 0.5 then slowly decrease from 0.5 and 1. These observations are confirmed by the PSNR- η curves (Figure 6). This experiment suggests that the noisier channel benefits from the less noisy one (best results obtained with $\eta = 0.5$). Conversely, the less noisy channel does not benefit much from the noisier one.

We performed a principal component analysis (PCA) on the latent variables z s obtained by encoding the training dataset image pairs (x_1, x_2) with the trained encoder. A target latent variable z^* was obtained by encoding the target image pair (x_1^*, x_2^*) from (16). Figure 7 shows a projection of the latent space onto the 2-dimensional (2-D) subspace spanned by the two first principal components. The blue crosses represent the \hat{z}^η latent variables corresponding to the denoised image pairs $(\hat{x}_1^\eta, \hat{x}_2^\eta)$ for different values of η . We observe that the distance to the target increases as η moves away from 1/2.

In conclusion of this experiment, we observe our MVAE regularizer manages denoise while conveying information between the two channels.

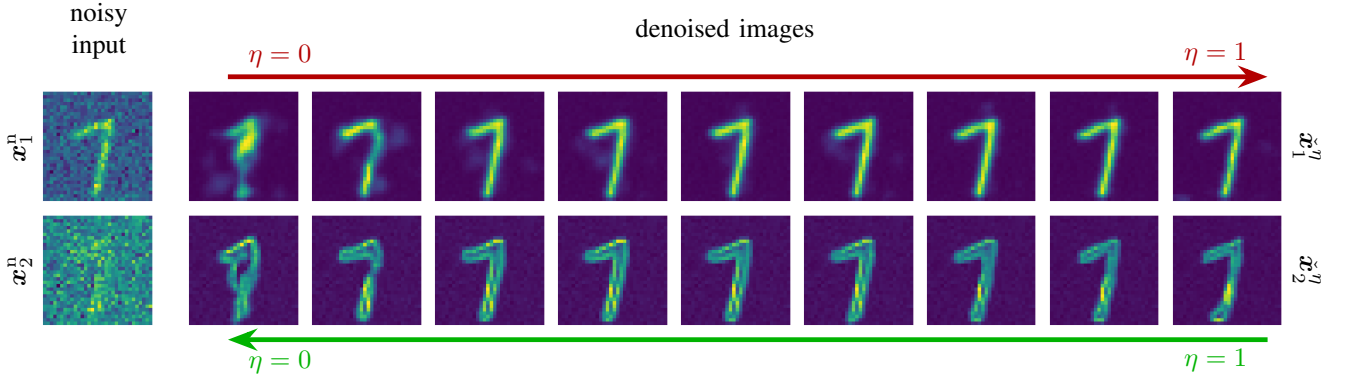


Fig. 5: Noisy images ($\mathbf{x}_1^n, \mathbf{x}_2^n$) and MVAE-denoised images ($\hat{\mathbf{x}}_1^\eta, \hat{\mathbf{x}}_2^\eta$) for different values of η ranging from 0.01 to 0.99 $\beta = 1$.

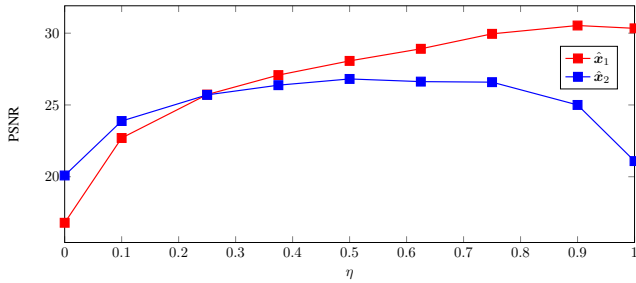


Fig. 6: PSNR values of denoised MNIST images using MVAE for a range of η values.

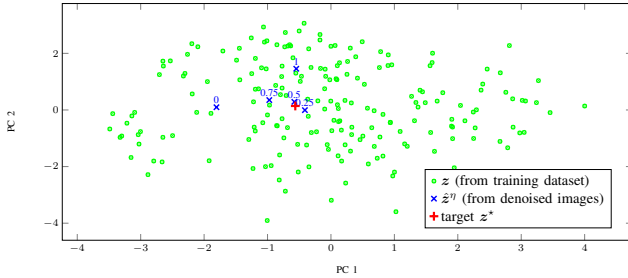
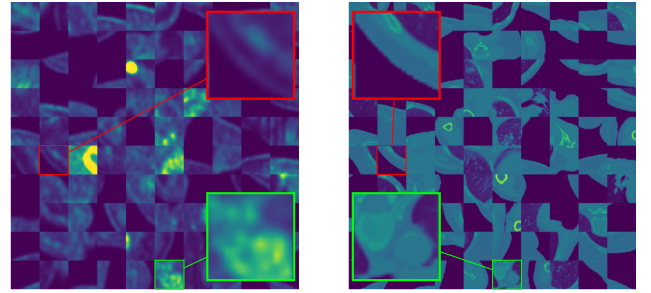


Fig. 7: 2-D representation of the latent space by PCA. The PCA was performed on the \mathbf{z} latent variables of the training dataset (green dots). The red cross corresponds to the target latent variable \mathbf{z}^* obtained by encoding the target pair ($\mathbf{x}_1^*, \mathbf{x}_2^*$) in (16). The blue crosses correspond to the latent variables $\hat{\mathbf{z}}^\eta$ from the denoised image pair ($\hat{\mathbf{x}}_1^\eta, \hat{\mathbf{x}}_2^\eta$) for $\eta \in \{0.1, 0.5, 0.75, 1\}$, the label on each blue cross corresponding to the η -value.

B. Synergistic PET/CT Reconstruction

1) *Data and Training*: A collection of 328 abdomen PET/CT image volumes were acquired by Siemens Biograph mCT PET/CT scanner at *Centre Hospitalier Universitaire Poitiers*, Poitiers, France. Each volume comprises a set of 512×512 slices (0.97-mm pixel size), for a total of 41,000 slices per modality. A $(\mathbf{x}_1, \mathbf{x}_2)$ pair correspond to a PET/CT slice pair (\mathbf{x}_1 for PET, \mathbf{x}_2 for CT). A total of 318 pairs were used for training while 10 pairs were used for testing—testing images and training images came from different patients.

64×64 patches were randomly extracted from each image $2 \cdot 10^5$ patch pairs $(\mathbf{u}_1, \mathbf{u}_2)$, see Figure 8 for an example of patch pairs) then were used to train the MVAE model \mathcal{G}_θ and



(a) PET training patches

(b) CT training patches

Fig. 8: Examples for PET/CT patch pairs, i.e., $\mathbf{u}_1, \mathbf{u}_2$ in (26), used to train the MVAE model.

to define R_θ (12). The PET and CT were normalized before training, and the two normalizing constants were incorporated in R_θ (12). The Adam optimizer was used for training with a learning rate of 10^{-4} and batch size of 4,096 for 1,000 epochs.

We used 10 PET/CT image pairs $(\mathbf{x}_1^*, \mathbf{x}_2^*)$ from 10 patients as GT images to test other MVAE reconstruction. Figure 9 shows the GT images for Patient 1 which we used as main example. The PET data $\mathbf{y}_1 \in \mathbb{R}^{n_1}$ and CT data $\mathbf{y}_2 \in \mathbb{R}^{n_2}$ were generated following (1) using $\bar{\mathbf{y}} = \bar{\mathbf{y}}_k$, $k = 1, 2$, where $\bar{\mathbf{y}}_1: \mathbb{R}^m \rightarrow \mathbb{R}^{n_1}$ and $\bar{\mathbf{y}}_2: \mathbb{R}^m \rightarrow \mathbb{R}^{n_2}$ are respectively the PET and CT forward models (cf. (2) and (3)), and n_1 and n_2 are respectively the number of PET lines of response and the number of CT beams. The systems were implemented with ASTRA [45] with $n_1 = 120 \times 512$ for the PET (parallel geometry) and $n_2 = 120 \times 750$ for the CT (standard fan beam geometry with 1.2-mm detector size, 600-mm origin-to-source and origin-to-detector distances).

The scanner data \mathbf{y}_1 and \mathbf{y}_2 were acquired with 2 settings: (i) high-count PET/low-count CT (HC-PET/LC-CT) with $\tau = 700$ and $I = 2,000$, and (ii) low-count PET/high-count CT (LC-PET/HC-CT) with $\tau = 10$ and $I = 1.4 \cdot 10^5$.

The 64×64 patch extractors \mathcal{P}_p were defined with 75% overlap along each axis. The attenuation correction factors were obtained from a scout reconstruction of the attenuation image \mathbf{x}_2 from \mathbf{y}_2 using an unregularized WLS reconstruction, then converted into 511-keV images using the method proposed by Oehmigen *et al.* [46].

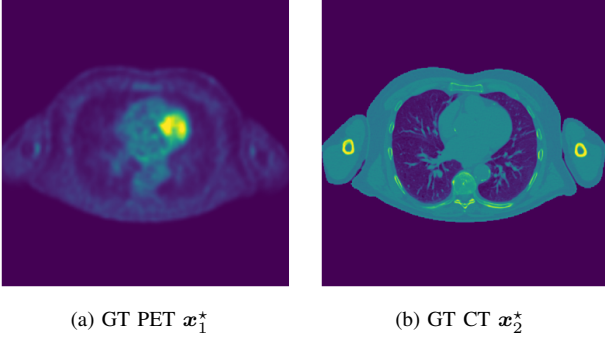


Fig. 9: First of the 10 testing PET/CT GT image pairs (x_1^*, x_2^*) used to generate the scanner raw data following (1).

The parameter β was finely tuned to optimize image quality in terms of PSNR and SSIM, and we used $\eta = 1/2$. The MVAE-reconstructed images are referred to MVAE-reconstructed PET (MVAE-PET) and MVAE-reconstructed CT (MVAE-CT).

Additionally, we implemented two other reconstruction techniques for comparison:

- The PLS approach proposed by Ehrhardt *et al.* [15] (the quadratic version) which consists of utilizing a synergistic penalty (i.e., R_{syn} in (6)) that promotes images with parallel gradient in order to enforce structural similarities between the images. We used a L-BFGS algorithm to perform the joint minimization in x_1 and x_2 . The reconstructed images are referred to as PLS-reconstructed PET (PLS-PET) and PLS-reconstructed CT (PLS-CT).
- MLEM PET reconstruction followed by U-Net denoising (MLEM-PET+UNet) and WLS CT reconstruction CT followed by U-Net denoising (WLS-CT+UNet), where both image-to-image U-Nets were trained to map low-count CT images to the GT images. The training of these methods is supervised and therefore they are expected to deliver better results.

Finally, we reconstructed the images using MLEM for PET and WLS for CT (using a SPS algorithm), which corresponds to MVAE with $\beta = 0$. The reconstructed images are referred to as MLEM-reconstructed PET (MLEM-PET) and WLS-reconstructed CT (WLS-CT).

2) Results:

a) Image Generation: Figure 10 shows random images of generated images patches using the trained MVAE PET/CT model, using a random z , in a similar fashion as for the MNIST-trained model (Section III-A2). The images generated from the PET generator $G_\theta^1(z)$ (Figure 10(a)) appear blurry while those generated from the CT generator $G_\theta^2(z)$ (Figure 10(b)) are sharper. Structural similarities can be observed (cf. the magnified areas in Figure 10), which suggests that information is shared between the two modalities. However, these similarities are less pronounced than the MNIST-trained model.

b) Image Reconstruction: High-count PET, Low-count CT: Figure 11 shows the images reconstructed from LC-PET/HC-CT simulated data (Patient 1). The MLEM-PET and WLS-CT images exhibit significant noise amplification. In contrast, MVAE-PET/MVAE-CT, PLS-PET/PLS-CT, and MLEM-PET+UNet/WLS-CT+UNet appear free of noise. This

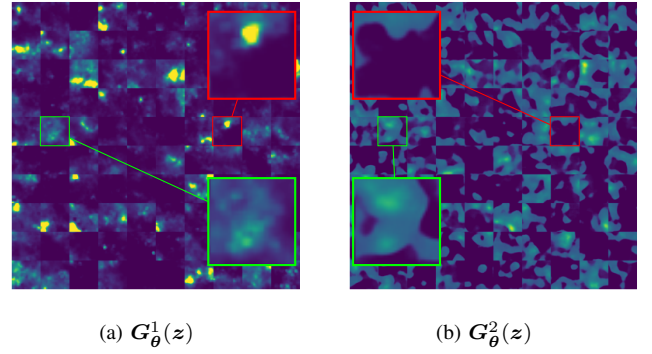


Fig. 10: MVAE-generated image pairs ($G_\theta^1(z), G_\theta^2(z)$) with random $z \in \mathcal{Z}$, using the PET/CT-trained models, with random $z \in \mathcal{Z}$. The sub-images on (a) and (b) at same position were generated from the same z .

	HC-PET				LC-CT			
	MVAE	PLS	U-Net	MLEM	MVAE	PLS	U-Net	WLS
PSNR	56.0524	60.0029	56.9691	55.3558	36.7953	37.0943	38.6244	30.0829
SSIM	0.9983	0.9994	0.9981	0.9976	0.9686	0.9766	0.9832	0.8807

TABLE I: HC-PET/LC-CT—Metric for each method averaged over the 10 patients.

example demonstrates that PLS outperforms MVAE on PET, while MVAE shows a slight advantage over PLS on CT. U-Net denoising surpasses all methods except PLS-PET, which achieves better SSIM than MLEM-PET+UNet. Reconstructed images of the nine other patients are shown in Figure 16 (Appendix A).

Figure 12 presents a scatter plot of SSIM versus PSNR for the 10 patients, comparing MVAE-PET/PLS-PET (Figure 12(a)) and MVAE-CT/PLS-CT (Figure 12(a)). To enhance visibility, MLEM-PET and WLS-CT were omitted, as they are significantly outperformed. Consistent with the observations from Figure 11, PLS-PET slightly outperforms MVAE-PET, achieving $\text{PSNR} \approx 56\text{--}64\text{ dB}$ and $\text{SSIM} \approx 0.999\text{--}0.9999$, compared to $\text{PSNR} \approx 51\text{--}59\text{ dB}$ and $\text{SSIM} \approx 0.997\text{--}0.999$ for MVAE-PET. Additionally, MLEM-PET+UNet shows a slight improvement over MVAE-PET in terms of PSNR ($\approx 54\text{--}60\text{ dB}$).

On the CT side, PLS-CT outperforms MVAE-CT, with both methods achieving comparable PSNR values ($\approx 35\text{--}39\text{ dB}$), but with SSIM values slightly favoring PLS-CT ($\text{SSIM} \approx 0.96\text{--}0.985$ for PLS-CT, compared to $\text{SSIM} \approx 0.96\text{--}0.98$ for MVAE-CT). The underperformance of MVAE-CT can be attributed to the tendency of VAE-based methods to produce blurry images, which are less suited for CT reconstruction. Finally, WLS-CT+UNet surpasses all other methods, as it is specifically trained to low-count CT images to the GT CT images.

Table I show the metrics averaged over the 10 patients.

c) Image Reconstruction: Low-count PET, High-count CT: Figure 13 shows the images obtained from LC-PET/HC-CT simulated data (Patient 1/10). Similarly to the HC-PET/LC-CT experiment, MLEM-PET and WLS-CT suffer from noise amplification (especially MLEM-PET) while MVAE-PET/MVAE-CT, PLS-PET/PLS-CT and MLEM-PET+UNet/WLS-CT+UNet appear noise-free. However this time MVAE outperforms PLS on the PET while PLS outperforms MVAE on the CT. MLEM-PET+UNet denoising outperforms all other methods on the PET but WLS-CT+UNet is outperformed by PLS-CT. Reconstructed

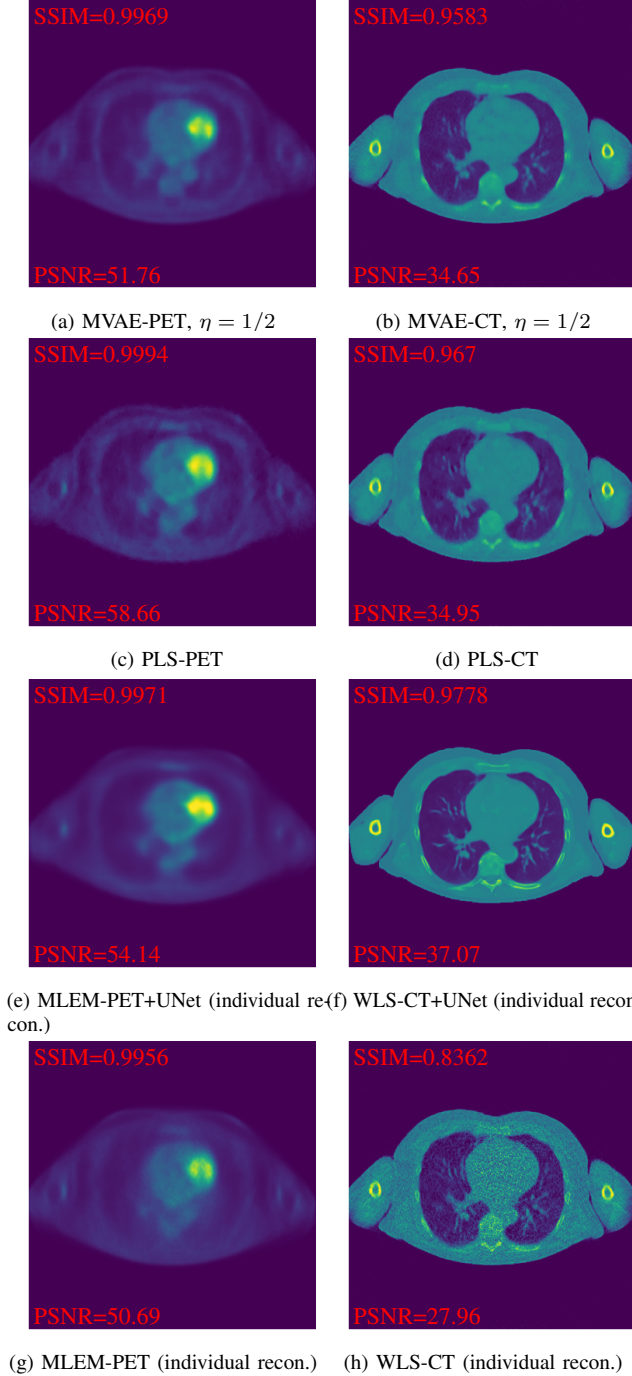


Fig. 11: HC-PET/LC-CT—Reconstructed PET/CT images using MVAE and PLS (PET/CT), MLEM (PET) and WLS (CT). MVAE-PET/MVAE-CT ((a) & (b)) and PLS-PET/PLS-CT ((c) & (d)) were reconstructed synergistically, while MLEM-PET+UNet and WLS-CT+UNet ((e) & (f)) as well as MLEM-PET+UNet and WLS-CT+UNet ((g) & (h)) were reconstructed individually. The GT images \mathbf{x}_1^* and \mathbf{x}_2^* are shown in Figure 9.

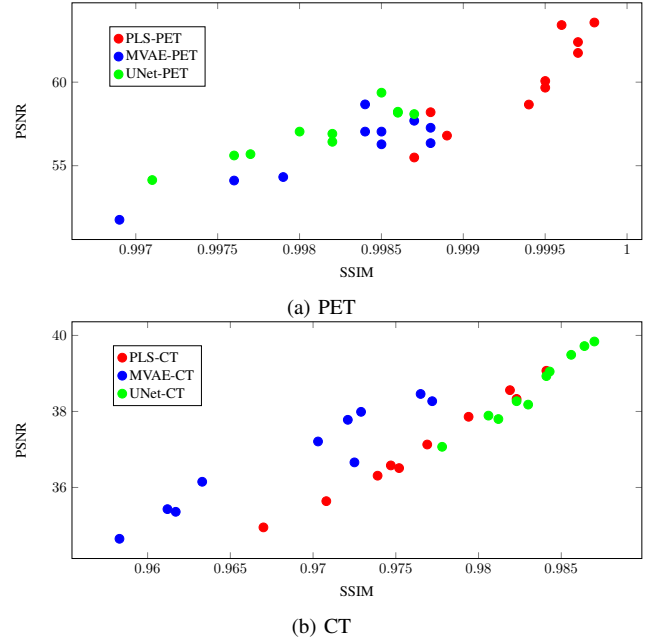


Fig. 12: HC-PET/LC-CT—PSNR vs SSIM scatter plot of the 10 PET/CT images reconstructed using MVAE and PLS: (a) reconstructed PET and (b) reconstructed CT.

images of the nine other patients are shown in Figure 17 (Appendix A).

In addition to this experiment, we assessed the ability of MVAE synergistic reconstruction to deal with mismatches between the PET and the CT data. For this purpose, we modified the GT PET image \mathbf{x}_1^* from Figure 9(a) by adding a 3-mm radius hot lesion s in the lung while keeping the GT CT \mathbf{x}_2^* untouched (Figure 9(b)), and we simulated projection data in the LC-PET/HC-CT setting. The MVAE-reconstructed images are shown in Figure 14. We observe that the hot lesion is present in the reconstructed PET image but is absent from the reconstructed CT image, with no evidence of crosstalks. This shows that use of separate branches for each modality allows the model to address the inconsistencies between PET and CT images. As a result, the MVAE model preserves unique from the PET while avoiding the introduction of artifacts in the CT.

Figure 15 shows the same scatter plot as Figure 12. MVAE outperforms PLS on the PET (PSNR \approx 52–57 dB & SSIM \approx 0.9975–0.999 for MVAE-PET, PSNR \approx 49–53 & SSIM \approx 0.994–0.997 for PLS-PET)—MLEM-PET+UNet gives the best results as it was trained to map low-dose PET images to GT PET images.

Regarding CT, PLS-CT gives the best results (PSNR \approx 38–42 & SSIM \approx 0.98–0.998) while MVAE-CT is on par with WLS-CT+UNet (PSNR \approx 37–41 & SSIM \approx 0.98–0.99), with the exception of Patient 1 for which MVAE-CT seems to underperform.

Table II show the metrics averaged over the 10 patients.

IV. DISCUSSION

This work follows up on our previous studies presented in [28], [29], where we initially trained our models on full images.

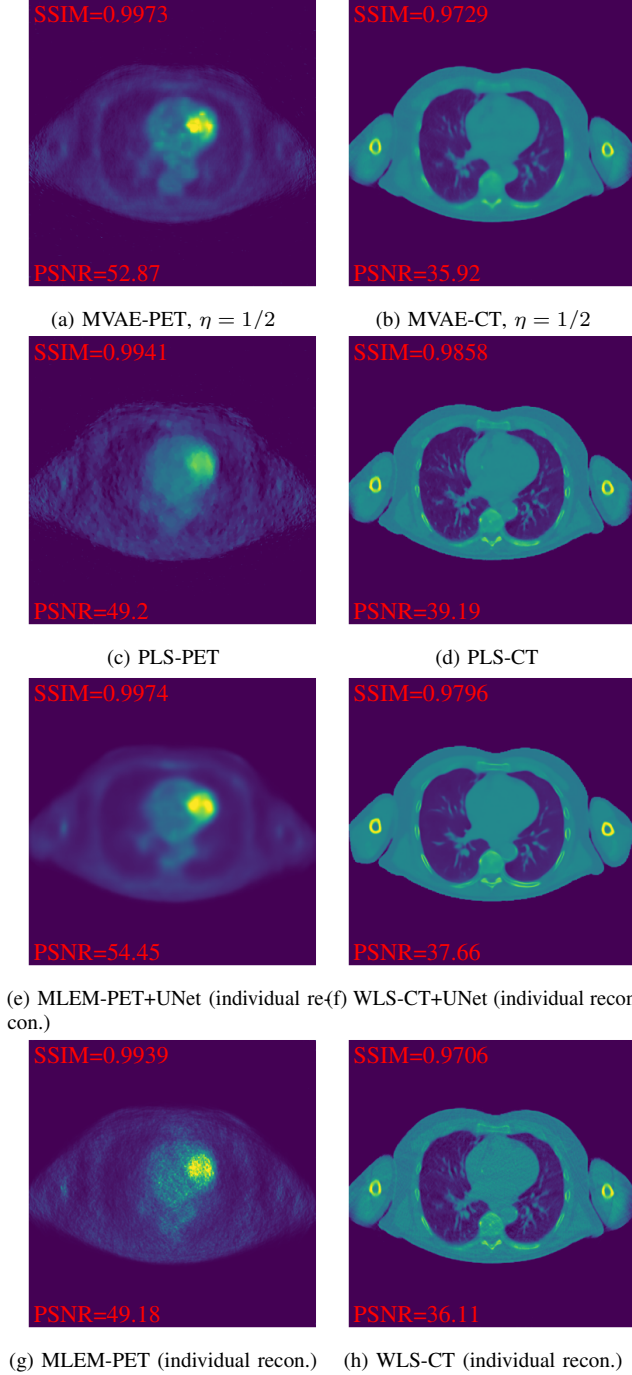
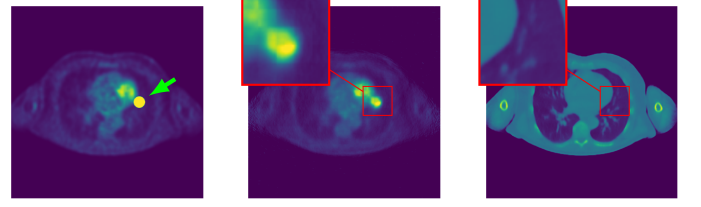


Fig. 13: LC-PET/HC-CT—Reconstructed PET/CT images using MVAE and PLS (PET/CT), MLEM (PET) and WLS (CT). MVAE-PET/MVAE-CT ((a) & (b)) and PLS-PET/PLS-CT ((c) & (d)) were reconstructed synergistically, while MLEM-PET+UNet and WLS-CT+UNet ((e) & (f)) as well as MLEM-PET and WLS-CT ((g) & (h)) were reconstructed individually. The GT images x_1^* and x_2^* are shown in Figure 9

	LC-PET				HC-CT			
	MVAE	PLS	U-Net	MLEM	MVAE	PLS	U-Net	WLS
PSNR	55.2722	51.6711	57.3095	52.4424	39.0144	40.4736	39.0674	39.4797
SSIM	0.9981	0.9957	0.9983	0.9964	0.9834	0.9892	0.9839	0.9824

TABLE II: LC-PET/HC-CT—Metric for each method averaged over the 10 patients.



(a) GT PET $x_1 + s$ (b) MVAE-PET, $\eta = 1/2$ (c) MVAE-CT, $\eta = 1/2$
 Fig. 14: LC-PET/HC-CT—PET/CT mismatch experiment: (a) GT PET with a lesion in the lung that is absent from the CT and the corresponding (b) MVAE-PET image and (c) MVAE-CT image.

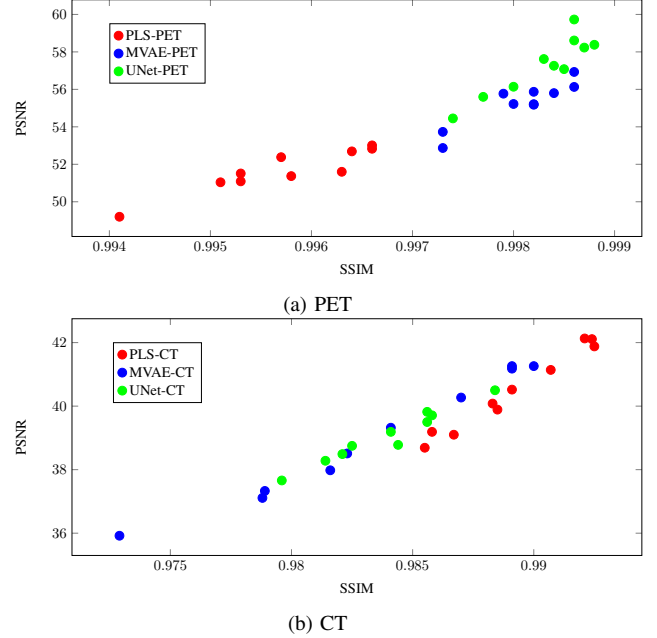


Fig. 15: LC-PET/HC-CT—PSNR vs SSIM scatter plot of the 10 PET/CT images reconstructed using MVAE and PLS: (a) reconstructed PET and (b) reconstructed CT.

However, we encountered potential overfitting issues due to the lack of data for training, resulting in overly optimistic results. To address this challenge, we adopted a patch decomposition approach. It has been previously reported that training on repetitive and consistent patches yields better results than training on the entire image [47]. To mitigate artifacts in the reconstructed images, our regularization strategy necessitates numerous overlapping patches. However, this comes at the expense of increased computational cost, as each patch requires its own latent variable. Besides, it is essential to remain vigilant about the potential for hallucinations. Future work may involve integrating more robust constraints and validation techniques to ensure the reliability and accuracy of the reconstructed images.

We demonstrated that our models successfully learn from two images simultaneously, suggesting their applicability for synergistic image reconstruction. Results obtained with MNIST-trained models distinctly showcase how our generative model-based regularizer effectively utilize information from both images for denoising.

Our HC-PET/LC-CT and LC-PET/HC-CT experiments

showed that MVAE outperforms the PLS technique [15] on low-count PET (although it is outperformed by PLS with high-count data), thus demonstrating that MVAE is suitable for low-dose imaging. However it is outperformed by U-Net denoising methods that are specifically trained to process this noise level.

The main drawback of VAEs is their tendency to generate blurry images. While this phenomenon has limited impact on PET due to its lower intrinsic resolution, it is more problematic for CT. In a previous version of this work, we implemented a multi-branch generative adversarial network which produced sharper images than those produced with MVAE, with the MNIST dataset. However the optimization with respect to the latent variable could not be achieved by L-BFGS and therefore we deployed a computationally expensive particle swarm optimization [48] (global optimizer). While this is reasonable with small images, it becomes unpractical if applied on a high number of patches.

Although we have demonstrated that multi-branch generative models offer a viable approach for learned synergistic reconstruction, it is important to explore alternative options beyond VAEs. Diffusion models (DMs) have shown significant promise in generating high-quality images from training datasets [49]. These models can be seamlessly integrated into a PML reconstruction framework, as demonstrated by diffusion posterior sampling (DPS) [50]. Recent advancements in spectral CT reconstruction have further highlighted the potential of DMs. More specifically, DMs are capable of capturing multi-channel information and employing multi-channel DPS leads to superior spectral CT images compared to conventional techniques [51], [52]. Therefore, the future of learned synergistic reconstruction may shift towards leveraging DMs.

V. CONCLUSION

In conclusion, our study highlights the utility of generative models for learned synergistic reconstruction in medical imaging. By training on pairs of images, our approach harnesses the power of VAEs to improve denoising and reconstruction outcomes. While challenges such as patch decomposition and inherent model limitations persist, our results demonstrate promising advancements in leveraging generative models for enhancing image quality and information exchange between modalities. Moving forward, further exploration of alternative models, such as DMs, may offer additional avenues for enhancing imaging outcomes in medical diagnostics and research. Overall, our findings contribute to the growing body of literature on learned synergistic reconstruction methods and pave the way for future developments in medical multimodal imaging technology.

APPENDIX A TRAINING OF THE MVAE

In this section we summarize the MVAE training strategy taking inspiration from Duff *et al.* [30] with a generalization the multichannel setting.

The K -channel patches from the training dataset are represented by a random array $\mathbf{U} = \{\mathbf{u}_k\} = \{\mathbf{u}_1, \dots, \mathbf{u}_K\} \in \mathcal{U}^K$,

such that for all k , $\mathbf{u}_k \in \mathcal{U}$ represents a patch in channel k . We denote by $p^*: \mathcal{U}^K \rightarrow \mathbb{R}^+$ the empirical probability distribution function (PDF) of \mathbf{U} , which corresponds to randomly selecting a patient image from the training dataset and extracting K patches (one patch per channel at the same location for all k). We assume the latent space \mathcal{Z} is endowed with a PDF $p_0: \mathcal{Z} \rightarrow \mathbb{R}^+$ (generally a standard normal PDF). The training consists in learning a parameter θ such that $\mathbf{G}_\theta^{\text{mult}}(\mathbf{z})$, $\mathbf{z} \sim p_0$, has a PDF that generalizes p^* such that it approximates the true PDF of \mathbf{U} . Denoting by $p_\theta: \mathcal{U}^K \rightarrow \mathbb{R}^+$ the probability distribution of $\mathbf{G}_\theta^{\text{mult}}(\mathbf{z})$, the training is achieved by minimizing a “distance” p^* and p_θ :

$$\min_{\theta} d(p^* || p_\theta) \quad (17)$$

For VAEs, the distance considered is the Kullback-Leibler divergence, denoted d_{KL} , which when applied to p^* and p_θ gives us

$$\begin{aligned} d_{\text{KL}}(p^* || p_\theta) &= \mathbb{E}_{\mathbf{U} \sim p^*} \left[\log \left(\frac{p^*(\mathbf{U})}{p_\theta(\mathbf{U})} \right) \right] \quad (18) \\ &= \mathbb{E}_{\mathbf{U} \sim p^*} [\log p^*(\mathbf{U})] - \mathbb{E}_{\mathbf{U} \sim p^*} [\log p_\theta(\mathbf{U})]. \quad (19) \end{aligned}$$

Minimizing $d_{\text{KL}}(p^* || p_\theta)$ is therefore equivalent to maximizing $\mathbb{E}_{\mathbf{U} \sim p^*} [\log p_\theta(\mathbf{U})]$.

The PDF p_θ is untractable and therefore we employ the following parametric inference model:

$$\mathbf{U} | \mathbf{z} \sim \mathcal{N}(\mathbf{G}_\theta(\mathbf{z}), \rho^2 \text{id}_{\mathcal{U}^K}) \quad (20)$$

$$\mathbf{z} | \mathbf{U} \sim \mathcal{N}(\boldsymbol{\mu}_\psi(\mathbf{U}), \text{diag}(\boldsymbol{\sigma}_\psi^2(\mathbf{U}))) \quad (21)$$

where $\boldsymbol{\mu}_\psi, \boldsymbol{\sigma}_\psi^2: \mathcal{U}^K \rightarrow \mathcal{Z}$ are respectively the multichannel *encoder mean* and multichannel *encoder variance* (parametrized by ψ), each of which mapping a K -channel patch $\mathbf{U} = \{\mathbf{u}_1, \dots, \mathbf{u}_K\}$ to a single latent variable. In our work, these encoders are built with $K = 2$ encoders whose output are merged (via a concatenation) into a single vector out of which the mean and variance vectors are generated (cf. left part of Figure 1). Denoting by $p_\theta(\cdot | \mathbf{z})$ and $q_\psi(\cdot | \mathbf{U})$ the conditional PDFs of $\mathbf{U} | \mathbf{z}$ and $\mathbf{z} | \mathbf{U}$ respectively, the PDF p_θ can be derived using the Bayes’ rule and marginalization as

$$p_\theta(\mathbf{U}) = \int_{\mathcal{Z}} \frac{p_\theta(\mathbf{U} | \mathbf{z}) p_0(\mathbf{z})}{q_\psi(\mathbf{z} | \mathbf{U})} q_\psi(\mathbf{z} | \mathbf{U}) d\mathbf{z} \quad (22)$$

$$= \mathbb{E}_{\mathbf{z} | \mathbf{U}} \left[\frac{p_\theta(\mathbf{U} | \mathbf{z}) p_0(\mathbf{z})}{q_\psi(\mathbf{z} | \mathbf{U})} \right]. \quad (23)$$

The log function being concave, we can derive the following maximizing the evidence lower bound (ELBO) for $\log p_\theta(\mathbf{U})$ using the Jensen inequality:

$$\log p_\theta(\mathbf{U}) \geq \mathbb{E}_{\mathbf{z} | \mathbf{U}} \left[\log \left(\frac{p_\theta(\mathbf{U} | \mathbf{z}) p_0(\mathbf{z})}{q_\psi(\mathbf{z} | \mathbf{U})} \right) \right] \quad (24)$$

$$= \mathbb{E}_{\mathbf{z} | \mathbf{U}} [p_\theta(\mathbf{U} | \mathbf{z}) - d_{\text{KL}}(q_\psi(\cdot | \mathbf{U}) || p_0)]. \quad (25)$$

Finally, an approximate minimizer of (19) can be obtain by minimizing the expectation of the negative ELBO, i.e.,

$$\begin{aligned} \min_{\theta, \psi} \mathbb{E}_{\mathbf{U} \sim p^*} \left[\mathbb{E}_{\mathbf{z} | \mathbf{U}} \left[\frac{1}{2\rho^2} \|\mathbf{U} - \mathbf{G}_\theta^{\text{mult}}(\mathbf{z})\|_2^2 \right] \right. \\ \left. + d_{\text{KL}} \{q_\psi(\cdot | \mathbf{U}) || p_0\} \right]. \quad (26) \end{aligned}$$

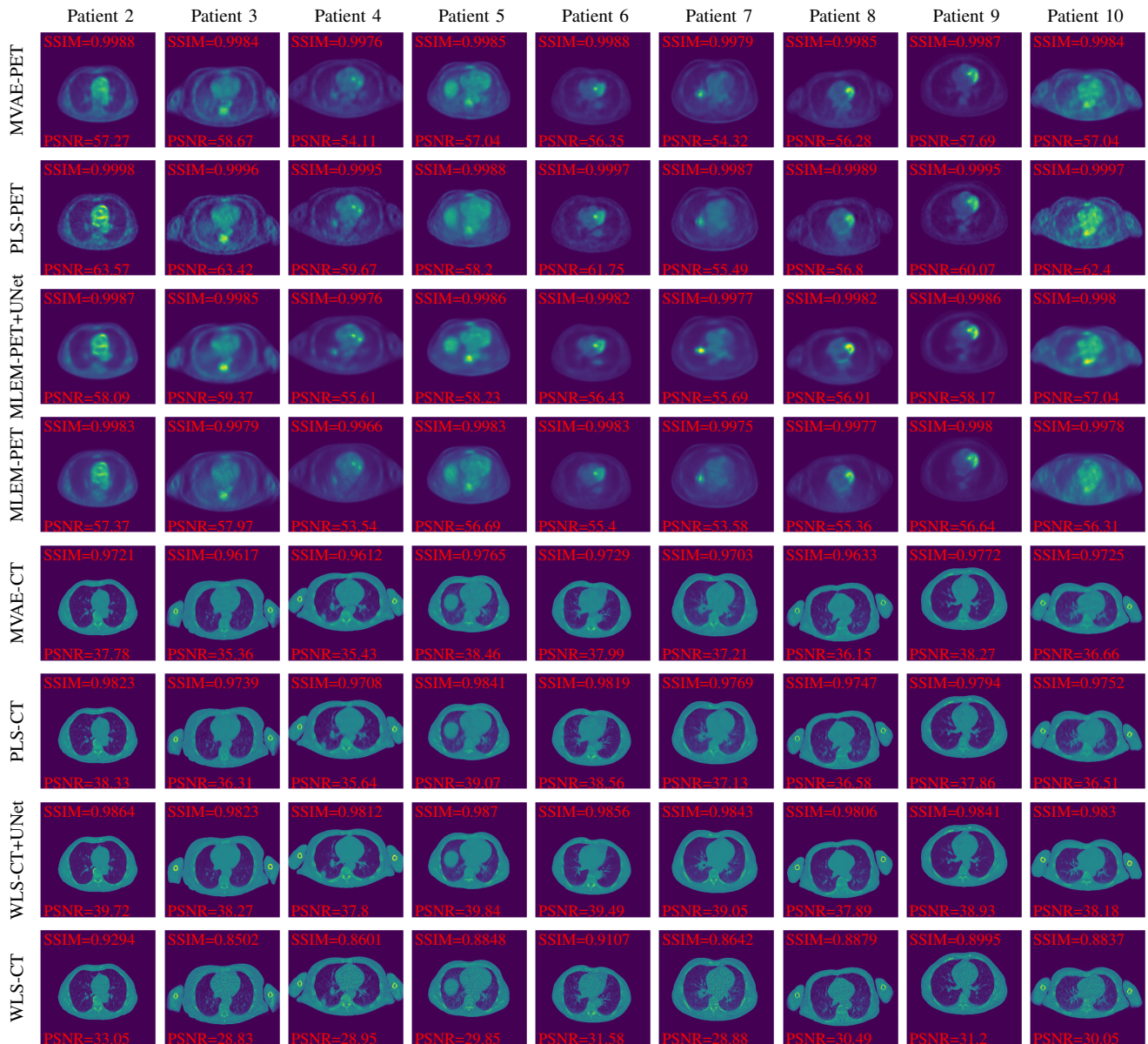


Fig. 16: HC-PET/LC-CT—Reconstructed images of the nine other patients.

APPENDIX B

ADDITIONAL RECONSTRUCTED IMAGES

In this appendix we display the reconstructed images for the nine other patient from data HC-PET/LC-CT data (Figure 16) and LC-PET/HC-CT data (Figure 17).

ACKNOWLEDGMENT

All authors declare that they have no known conflicts of interest in terms of competing financial interests or personal relationships that could have an influence or are relevant to the work reported in this paper.

REFERENCES

- [1] L. Gómez-Chova, D. Tuia, G. Moser, and G. Camps-Valls, “Multi-modal classification of remote sensing images: A review and future directions,” *Proceedings of the IEEE*, vol. 103, no. 9, pp. 1560–1584, 2015. DOI: 10.1109/JPROC.2015.2449668.
- [2] M. Dalla Mura, S. Prasad, F. Pacifici, P. Gamba, J. Chanussot, and J. A. Benediktsson, “Challenges and opportunities of multimodality and data fusion in remote sensing,” *Proceedings of the IEEE*, vol. 103, no. 9, pp. 1585–1601, Sep. 2015, ISSN: 0018-9219, 1558-2256. DOI: 10.1109/JPROC.2015.2462751.
- [3] T. Xue, W. Wang, J. Ma, W. Liu, Z. Pan, and M. Han, “Progress and prospects of multimodal fusion methods in physical human–robot interaction: A review,” *IEEE Sensors Journal*, vol. 20, no. 18, pp. 10355–10370, 2020. DOI: 10.1109/JSEN.2020.2995271.
- [4] H. Su, W. Qi, J. Chen, C. Yang, J. Sandoval, and M. A. Laribi, “Recent advancements in multimodal human–robot interaction,” *Frontiers in Neurobotics*, vol. 17, p. 1084000, May 2023, ISSN: 1662-5218. DOI: 10.3389/fnbot.2023.1084000.
- [5] B. J. Pichler, M. S. Judenhofer, and C. Pfannenber, “Multimodal imaging approaches: PET/CT and PET/MRI,” *en*, in *Molecular Imaging I* (Handbook of Experimental Pharmacology), W. Semmler and M. Schwaiger, Eds., Handbook of Experimental Pharmacology. Berlin, Heidelberg: Springer Berlin Heidelberg, 2008, vol. 185/1, pp. 109–132, ISBN: 978-3-540-72717-0. DOI: 10.1007/978-3-540-72717-7_6.

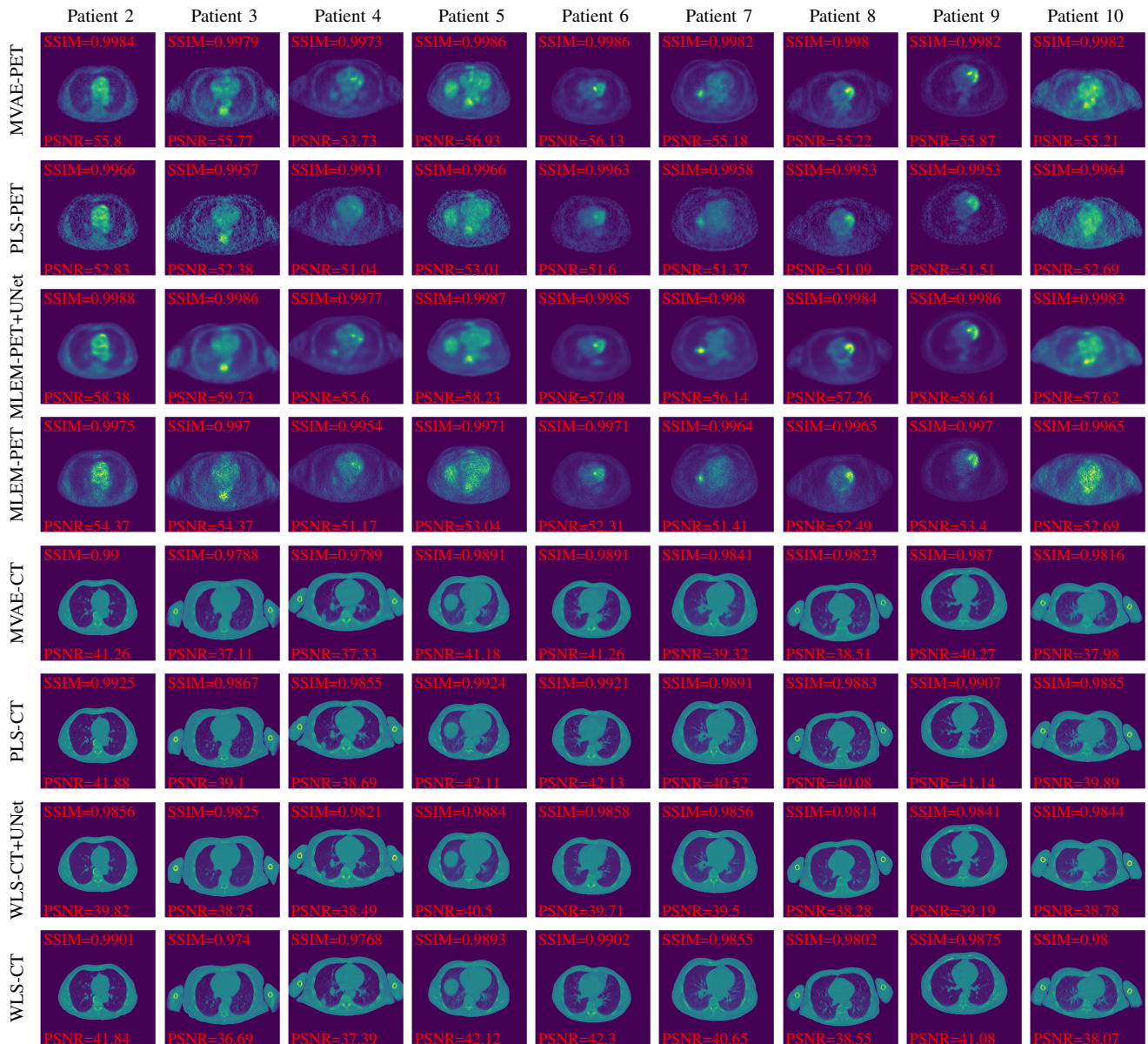


Fig. 17: LC-PET/HC-CT—Reconstructed images of the nine other patients.

- [Online]. Available: http://link.springer.com/10.1007/978-3-540-72718-7_6.
- [6] P. Decazes, P. Hinault, O. Veresezan, S. Thureau, P. Gouel, and P. Vera, "Trimodality PET/CT/MRI and radiotherapy: A mini-review," *Frontiers in Oncology*, vol. 10, p. 614008, Feb. 2021, ISSN: 2234-943X. DOI: 10.3389/fonc.2020.614008.
- [7] D. L. Bailey, M. N. Maisey, D. W. Townsend, and P. E. Valk, *Positron emission tomography*. Springer, 2005, vol. 2.
- [8] F. Natterer, *The mathematics of computerized tomography*. SIAM, 2001.
- [9] L. A. Shepp and Y. Vardi, "Maximum likelihood reconstruction for emission tomography," *IEEE Transactions on Medical Imaging*, vol. 1, no. 2, pp. 113–122, 1982. DOI: 10.1109/TMI.1982.4307558.
- [10] P. J. Green, "Bayesian reconstructions from emission tomography data using a modified em algorithm," *IEEE transactions on medical imaging*, vol. 9, no. 1, pp. 84–93, 1990.
- [11] A. R. De Pierro, "A modified expectation maximization algorithm for penalized likelihood estimation in emission tomography," *IEEE transactions on medical imaging*, vol. 14, no. 1, pp. 132–137, 1995.
- [12] I. A. Elbakri and J. A. Fessler, "Statistical image reconstruction for polyenergetic X-ray computed tomography," *IEEE transactions on medical imaging*, vol. 21, no. 2, pp. 89–99, 2002.
- [13] P. Blomgren and T. F. Chan, "Color TV: Total variation methods for restoration of vector-valued images," *IEEE transactions on image processing*, vol. 7, no. 3, pp. 304–309, 1998.
- [14] A. Mehranian, M. A. Belzunce, C. Prieto, A. Hammers, and A. J. Reader, "Synergistic PET and SENSE MR image reconstruction using joint sparsity regularization," *IEEE transactions on medical imaging*, vol. 37, no. 1, pp. 20–34, 2017.
- [15] M. J. Ehrhardt, K. Thielemans, L. Pizarro, D. Atkinson, S. Ourselin, B. F. Hutton, and S. R. Arridge, "Joint reconstruction of PET-MRI by exploiting structural similarity," *Inverse Problems*, vol. 31, no. 1, p. 015001, 2014.
- [16] D. S. Rigie and P. J. La Rivière, "Joint reconstruction of multi-channel, spectral CT data via constrained total nuclear variation minimization," *Physics in Medicine & Biology*, vol. 60, no. 5, p. 1741, 2015.
- [17] S. R. Arridge, M. J. Ehrhardt, and K. Thielemans, "(an overview of) synergistic reconstruction for multimodality/multichannel imaging

- methods," *Philosophical Transactions of the Royal Society A*, vol. 379, no. 2200, p. 20200205, 2021.
- [18] B. A. Thomas, V. Cuplov, A. Bousse, A. Mendes, K. Thielemans, B. F. Hutton, and K. Erlandsson, "PETPVC: A toolbox for performing partial volume correction techniques in positron emission tomography," *Physics in Medicine & Biology*, vol. 61, no. 22, p. 7975, 2016.
- [19] Q. Xu, H. Yu, X. Mou, L. Zhang, J. Hsieh, and G. Wang, "Low-dose X-ray CT reconstruction via dictionary learning," *IEEE transactions on medical imaging*, vol. 31, no. 9, pp. 1682–1697, 2012.
- [20] Y. Zhang, X. Mou, G. Wang, and H. Yu, "Tensor-based dictionary learning for spectral CT reconstruction," *IEEE transactions on medical imaging*, vol. 36, no. 1, pp. 142–154, 2016.
- [21] Y. Zhang, Y. Xi, Q. Yang, W. Cong, J. Zhou, and G. Wang, "Spectral CT reconstruction with image sparsity and spectral mean," *IEEE transactions on computational imaging*, vol. 2, no. 4, pp. 510–523, 2016.
- [22] W. Wu, Y. Zhang, Q. Wang, F. Liu, P. Chen, and H. Yu, "Low-dose spectral CT reconstruction using image gradient ℓ_0 -norm and tensor dictionary," *Applied Mathematical Modelling*, vol. 63, pp. 538–557, 2018.
- [23] X. Li, X. Sun, Y. Zhang, J. Pan, and P. Chen, "Tensor dictionary learning with an enhanced sparsity constraint for sparse-view spectral CT reconstruction," in *Photonics*, MDPI, vol. 9, 2022, p. 35.
- [24] A. Bousse, V. S. S. Kandarpa, S. Rit, A. Perelli, M. Li, G. Wang, J. Zhou, and G. Wang, "Systematic review on learning-based spectral CT," *IEEE Transactions on Radiation and Plasma Medical Sciences*, 2023. DOI: 10.1109/TRPMS.2023.3314131. [Online]. Available: <https://arxiv.org/abs/2304.07588>.
- [25] V. P. Sudarshan, G. F. Egan, Z. Chen, and S. P. Awate, "Joint PET-MRI image reconstruction using a patch-based joint-dictionary prior," *Medical image analysis*, vol. 62, p. 101669, 2020.
- [26] A. Perelli, S. A. Garcia, A. Bousse, J.-P. Tasu, N. Efthimiadis, and D. Visvikis, "Multi-channel convolutional analysis operator learning for dual-energy CT reconstruction," *Physics in Medicine & Biology*, vol. 67, no. 6, p. 065001, 2022.
- [27] G. Corda-D'Incan, J. A. Schnabel, A. Hammers, and A. J. Reader, "Single-modality supervised joint PET-MR image reconstruction," *IEEE Transactions on Radiation and Plasma Medical Sciences*, 2023.
- [28] N. J. Pinton, A. Bousse, Z. Wang, C. Cheze-Le-Rest, V. Maxim, C. Comtat, F. Sureau, and D. Visvikis, "Synergistic PET/CT reconstruction using a joint generative model," in *International Conference on Fully Three-Dimensional Image Reconstruction in Radiology and Nuclear Medicine*, 2023.
- [29] N. J. Pinton, A. Bousse, C. Cheze-Le-Rest, and D. Visvikis, "Joint PET/CT reconstruction using a double variational autoencoder," in *IEEE Nuclear Science Symposium Medical Imaging Conference and Room Temperature Semiconductor Conference*, 2023.
- [30] M. Duff, N. D. Campbell, and M. J. Ehrhardt, "Regularising inverse problems with generative machine learning models," *arXiv preprint arXiv:2107.11191*, 2021.
- [31] V. A. Kelkar and M. Anastasio, "Prior image-constrained reconstruction using style-based generative models," in *International Conference on Machine Learning*, PMLR, 2021, pp. 5367–5377.
- [32] L. Deng, "The MNIST database of handwritten digit images for machine learning research [best of the web]," *IEEE signal processing magazine*, vol. 29, no. 6, pp. 141–142, 2012.
- [33] H. M. Hudson and R. S. Larkin, "Accelerated image reconstruction using ordered subsets of projection data," *IEEE Transactions on Medical Imaging*, vol. 13, no. 4, pp. 601–609, 1994.
- [34] E. Y. Sidky, J. H. Jørgensen, and X. Pan, "Convex optimization problem prototyping for image reconstruction in computed tomography with the Chambolle–Pock algorithm," *Physics in Medicine & Biology*, vol. 57, no. 10, p. 3065, 2012.
- [35] S. R. Arridge, P. Maass, O. Öktem, and C.-B. Schönlieb, "Solving inverse problems using data-driven models," *Acta Numerica*, vol. 28, pp. 1–174, 2019.
- [36] V. Monga, Y. Li, and Y. C. Eldar, "Algorithm unrolling: Interpretable, efficient deep learning for signal and image processing," *IEEE Signal Processing Magazine*, vol. 38, no. 2, pp. 18–44, 2021.
- [37] V. S. S. Kandarpa, A. Bousse, D. Benoit, and D. Visvikis, "DUG-RECON: A framework for direct image reconstruction using convolutional generative networks," *IEEE Transactions on Radiation and Plasma Medical Sciences*, vol. 5, no. 1, pp. 44–53, Jan. 2021, arXiv:2012.02000 [physics], ISSN: 2469-7311, 2469-7303. DOI: 10.1109/TRPMS.2020.3033172.
- [38] R. Ma, J. Hu, H. Sari, S. Xue, C. Mingels, M. Viscione, V. S. S. Kandarpa, W. B. Li, D. Visvikis, R. Qiu, A. Rominger, J. Li, and K. Shi, "An encoder-decoder network for direct image reconstruction on sinograms of a long axial field of view PET," *Eur J Nucl Med Mol Imaging*, vol. 49, no. 13, pp. 4464–4477, Jul. 2022.
- [39] Z. Cao and L. Xu, "12 - direct image reconstruction in electrical tomography and its applications," in *Industrial Tomography (Second Edition)* (Woodhead Publishing Series in Electronic and Optical Materials), M. Wang, Ed., Second Edition, Woodhead Publishing Series in Electronic and Optical Materials, Woodhead Publishing, 2022, pp. 389–425, ISBN: 978-0-12-823015-2. DOI: <https://doi.org/10.1016/B978-0-12-823015-2.00018-2>. [Online]. Available: <https://www.sciencedirect.com/science/article/pii/B9780128230152000182>.
- [40] Z. Wang, A. Bousse, F. Vermet, J. Froment, B. Vedel, A. Perelli, J.-P. Tasu, and D. Visvikis, "Uconnect: Synergistic spectral CT reconstruction with U-Nets connecting the energy bins," *IEEE Transactions on Radiation and Plasma Medical Sciences*, vol. 8, no. 2, pp. 222–233, 2024. DOI: 10.1109/TRPMS.2023.3330045. [Online]. Available: <https://arxiv.org/abs/2311.00666>.
- [41] A. F. Agarap, "Deep learning using rectified linear units (relu)," *arXiv preprint arXiv:1803.08375*, 2018.
- [42] A. De Pierro, "A modified expectation maximization algorithm for penalized likelihood estimation in emission tomography," *IEEE Transactions on Medical Imaging*, vol. 14, no. 1, pp. 132–137, 1995.
- [43] C. Zhu, R. H. Byrd, P. Lu, and J. Nocedal, "Algorithm 778: L-BFGS-B: Fortran subroutines for large-scale bound-constrained optimization," *ACM Transactions on mathematical software (TOMS)*, vol. 23, no. 4, pp. 550–560, 1997.
- [44] S. Van der Walt, J. L. Schönberger, J. Nunez-Iglesias, F. Boulogne, J. D. Warner, N. Yager, E. Guillard, and T. Yu, "Scikit-image: Image processing in Python," *PeerJ*, vol. 2, e453, 2014.
- [45] W. van Aarle, W. J. Palenstijn, J. Cant, E. Janssens, F. Bleichrodt, A. Dabrovolski, J. D. Beenhouwer, K. J. Batenburg, and J. Sijbers, "Fast and flexible x-ray tomography using the ASTRA toolbox," *Opt. Express*, vol. 24, no. 22, pp. 25 129–25 147, 2016. [Online]. Available: <http://opg.optica.org/oe/abstract.cfm?URI=oe-24-22-25129>.
- [46] M. Oehmigen, M. E. Lindemann, L. Tellmann, T. Lanz, and H. H. Quick, "Improving the CT (140 kvp) to PET (511 keV) conversion in PET/MR hardware component attenuation correction," in *Medical Physics*, vol. 47, no. 5, pp. 2116–2127, May 2020, ISSN: 0094-2405, 2473-4209. DOI: 10.1002/mp.14091.
- [47] K. Gupta, S. Singh, and A. Shrivastava, "PatchVAE: Learning local latent codes for recognition," in *Proceedings of the IEEE/CVF Conference on Computer Vision and Pattern Recognition*, 2020, pp. 4746–4755.
- [48] J. Kennedy and R. Eberhart, "Particle swarm optimization," in *Proceedings of ICNN'95 - International Conference on Neural Networks*, vol. 4, 1995, pp. 1942–1948. DOI: 10.1109/ICNN.1995.488968.
- [49] P. Dhariwal and A. Nichol, "Diffusion models beat GANs on image synthesis," *Advances in neural information processing systems*, vol. 34, pp. 8780–8794, 2021.
- [50] H. Chung, J. Kim, M. T. Mccann, M. L. Klasky, and J. C. Ye, "Diffusion posterior sampling for general noisy inverse problems," in *The Eleventh International Conference on Learning Representations*, 2023.
- [51] C. Vazia, A. Bousse, B. Vedel, F. Vermet, Z. Wang Zhihan Wang, T. Dassow, J.-P. Tasu, D. Visvikis, and J. Froment, "Diffusion posterior sampling for synergistic reconstruction in spectral computed tomography," in *2024 IEEE 21st international symposium on biomedical imaging (ISBI 2024)*, IEEE, 2024. [Online]. Available: <https://arxiv.org/abs/2403.06308>.
- [52] C. Vazia, A. Bousse, J. Froment, B. Vedel, F. Vermet, Z. Wang, T. Dassow, J.-P. Tasu, and D. Visvikis, "Spectral CT two-step and one-step material decomposition using diffusion posterior sampling," in *arXiv preprint arXiv:2403.10183*, 2024. [Online]. Available: <https://arxiv.org/abs/2403.10183>.